Advances in Applied Mathematics and Mechanics
Adv. Appl. Math. Mech., Vol. **4**, No. 4, pp. 439-453

DOI: 10.4208/aamm.10-m11158
August 2012

Numerical Simulation of a Multi-Frequency Resistivity Logging-While-Drilling Tool Using a Highly Accurate and Adaptive Higher-Order Finite Element Method

Zhonghua Ma[1,2], Dejun Liu[1,*], Hui Li[1] and Xinsheng Gao[1]

[1] *College of Geophysics and Information Engineering, China University of Petroleum, 18 Fuxue Road, Changping District, Beijing 102249, China*
[2] *LandOcean Energy Services Co., Ltd, Beijing 100084, China*

Received 14 October 2011; Accepted (in revised version) 16 November 2011
Available online 10 July 2012

Abstract. A novel, highly efficient and accurate adaptive higher-order finite element method (*hp*-FEM) is used to simulate a multi-frequency resistivity logging-while-drilling (LWD) tool response in a borehole environment. Presented in this study are the vector expression of Maxwell's equations, three kinds of boundary conditions, stability weak formulation of Maxwell's equations, and automatic *hp*-adaptivity strategy. The new *hp*-FEM can select optimal refinement and calculation strategies based on the practical formation model and error estimation. Numerical experiments show that the new *hp*-FEM has an exponential convergence rate in terms of relative error in a user-prescribed quantity of interest against the degrees of freedom, which provides more accurate results than those obtained using the adaptive *h*-FEM. The numerical results illustrate the high efficiency and accuracy of the method at a given LWD tool structure and parameters in different physical models, which further confirm the accuracy of the results using the Hermes library (`http://hpfem.org/hermes`) with a multi-frequency resistivity LWD tool response in a borehole environment.

AMS subject classifications: 35Q61, 35Q86, 74S05

Key words: Resistivity logging-while-drilling, higher-order finite element method, adaptive, exponential convergence, numerical simulation.

1 Introduction

Resistivity logging-while-drilling (LWD) is an electrical logging tool that plays an im-

*Corresponding author.
URL: `http://cii.cup.edu.cn/Showteacher.aspx?id=liudejun`
Email: mazhonghua1983@yahoo.com.cn (Z. H. Ma), liudj01@yahoo.com.cn (D. J. Liu), toobage@163.com (H. Li), shengxingao@163.com (X. S. Gao)

portant role in oil exploration [1, 2]. At present, resistivity LWD has become a key technology in data collection in real-time well fields, interpretation and field decision-making, and guiding geology-oriented drilling [3–7]. With the extensive application of resistivity LWD, analog simulation to resistivity LWD instrument response has become a hotspot in current research, in which one of the major works is to calculate electric potential and electric field strength in different physical models. It conducts the work via the theory of a self-adaptive higher-order finite element method (hp-FEM), establishment of mathematical and physical models, and research on logging response using a self-adaptive hp-FEM [8–10], around the core of multi-frequency resistivity LWD, in the light of difficult problems in conventional resistivity logging and thin layer logging.

Based on Maxwell's equations, the current paper derives the normalized time-harmonic Maxwell's equations through the rectangular coordinate system, presents three kinds of boundary conditions used in model and stability variation equation of Maxwell's equations, and discusses the high accuracy and efficiency of the self-adaptive hp algorithm. In addition, the optimal hp refinement strategy of elements and implementation of the new hp-FEM are discussed, and two structural parameters used by the numerical model for numerical simulations are presented using the structure of the classical single-emission and double-receiving logging instrument. In the single-layer formation model, the relationship between electric field resistivity and signal amplitude is calculated by matching the results well with the actual situation of works, which indicates feasibility of the proposed algorithm and numerical model structure in calculating resistivity LWD response under different frequencies. In the multi-layer formation model, the effects of different frequencies on the real part, imaginary part, amplitude, phase angle, first difference value of amplitude, wall rock, and wall rock thin layer are analyzed. The resistivity LWD response curves under different frequencies are also provided.

The electric field distribution in resistivity LWD under different frequencies is simulated and analyzed using the hp-FEM library Hermes. The corresponding relationships between the complex media of formation and formation electric field distribution are reflected by establishing a theoretical model, which is highly significant to obtain the instrument response simulation curve, guiding design of a highly accurate resistivity LWD instrument, and logging data processing and interpretation.

2 Model

The 2D cross-section diagram of the resistivity LWD instrument in a borehole environment is shown in Fig. 1. The model is composed of a resistivity logging instrument, non-vacuum borehole, and five layers in the formation material with varying resistivities. The resistivity logging tool is used as the classical single-emission and double-receiving structure. The main parameters are as follows:

- Length of transmitting coil (0.1m);

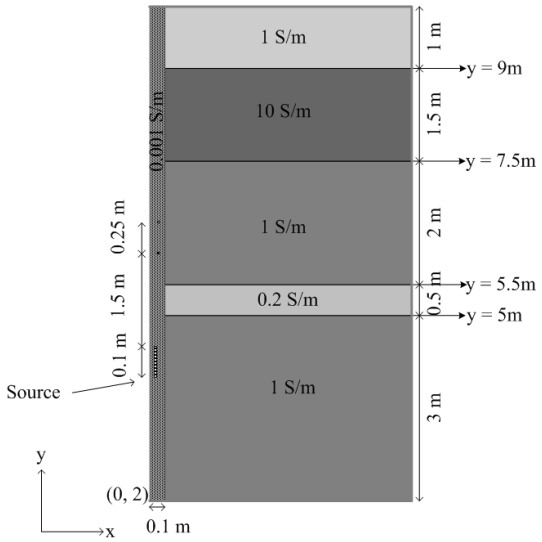

Figure 1: Geometry of the LWD problem. The model consists of one transmitter, two receiver coils, a conductive borehole, and five layers in the formation material with varying resistivities.

- Location of the first receiver coil above the transmitting coil (1.5m);
- Location of the second receiver coil above the transmitting coil (1.75m);
- Load current amplitude of the field source (0.3A);
- Borehole radius (0.1m);
- Borehole electrical conductivity (0.001S/m);
- Formation thicknesses from bottom to top (3, 0.5, 2, 1.5 and 1m, respectively);
- Electrical conductivities of formation from bottom to top (1, 0.2, 1, 10 and 1S/m, respectively).

2.1 Underlying PDE system

Maxwell's equations can be classified as either transverse electric (TE) or transverse magnetic (TM) models. Solving the problem in electric field is actually solving the problem of the Maxwell's equations under given boundary conditions.

The mathematical model of electromagnetic field is mainly composed of four laws. For practical purposes, these integral Maxwell's equations are transformed into partial differential equations using the Gauss's and Stokes's theorems. Based on these theorems, the following Maxwell's equations in differential forms are derived:

$$\nabla \times \boldsymbol{H} = \boldsymbol{J} + \frac{\partial \boldsymbol{D}}{\partial t}, \tag{2.1a}$$

$$\nabla \times \boldsymbol{E} = -\frac{\partial \boldsymbol{B}}{\partial t}, \tag{2.1b}$$

$$\nabla \cdot \boldsymbol{D} = \rho, \tag{2.1c}$$

$$\nabla \cdot \boldsymbol{B} = 0, \tag{2.1d}$$

where $\boldsymbol{E}$ is the electric field strength, $\boldsymbol{D}$ is the electric flux density, $\boldsymbol{H}$ is the magnetic field strength, $\boldsymbol{B}$ is the magnetic flux density, $\boldsymbol{J}$ is the current density, and ρ is the electric charge density. All material parameters are determined through the following constitutive relationships:

$$\boldsymbol{D} = \varepsilon \boldsymbol{E}, \tag{2.2a}$$

$$\boldsymbol{B} = \mu \boldsymbol{H}, \tag{2.2b}$$

$$\boldsymbol{J} = \gamma \boldsymbol{E} + \boldsymbol{J}_a, \tag{2.2c}$$

where the constitutive parameters electric permittivity ε, magnetic permittivity μ, electric conductivity γ are the physical properties of materials in the electromagnetic field and $\boldsymbol{J}_a$ is the applied current density. After the constitutive relationships among field quantities are determined, the Maxwell's equations are transformed into fixed solution forms. Electromagnetic properties depend on the position in the domain and can be discontinuous at the interfaces between different media. Therefore, the single hyperbolic equation for electric field is

$$\nabla \times (\mu^{-1} \nabla \times \boldsymbol{E}) + \gamma \frac{\partial \boldsymbol{E}}{\partial t} + \varepsilon \frac{\partial^2 \boldsymbol{E}}{\partial t^2} = -\frac{\partial \boldsymbol{J}_a}{\partial t}. \tag{2.3}$$

All quantities from Eq. (2.1a) to Eq. (2.1d) are often time-harmonic with the same angular frequency ω

$$\boldsymbol{E}(x,t) = \mathrm{Re}(\underline{\boldsymbol{E}}(x) e^{i\omega t}), \tag{2.4}$$

Eq. (2.4) can be used to eliminate all time derivatives. This can be formally done by substituting

$$\frac{\partial \boldsymbol{E}}{\partial t} = i\omega \boldsymbol{E}, \qquad \frac{\partial^2 \boldsymbol{E}}{\partial t^2} = -\omega^2 \boldsymbol{E},$$

and using $\mu = \mu_0 \mu_r$, $\varepsilon = \varepsilon_0 \varepsilon_r$ into Eq. (2.3). Finally, we obtain the normalized Maxwell's equation

$$\nabla \times (\mu_r^{-1} \nabla \times \boldsymbol{E}) - \left(k^2 \varepsilon_r - i\gamma k \sqrt{\frac{\mu_0}{\varepsilon_0}} \right) \boldsymbol{E} = -i\omega \boldsymbol{J}_a, \tag{2.5}$$

where $\boldsymbol{E} = \boldsymbol{E}(x,t)$ is the form of complex vector-valued phasor of the time-harmonic electric field strength and $k = \omega/c$ is the wave number.

2.2 Boundary conditions

Fig. 1 shows that the physical model used in the present study is a vertical well model. The transmitting coil is modeled with an impressed surface current prescribed on the coil boundary. The component $\boldsymbol{J}_s^{imp}$ of the surface current is usually not zero in the

electromagnetic field analysis. The infinite domain could be reduced to a computational rectangular domain because of an exponential decay of the solution [11]. The tangential component of the electric field could be set to zero using the perfect conductor boundary condition

$$\boldsymbol{E}\cdot\boldsymbol{t}=0, \tag{2.6}$$

where t is the tangential vector.

The vector-valued surface current $\boldsymbol{J}_s^{imp}$ loaded by the transmitting coil can be simplified to $\boldsymbol{J}_S$ and established through the Neumann boundary condition

$$\boldsymbol{n}\times(\mu_r^{-1}\nabla\times\boldsymbol{E})=i\omega\boldsymbol{J}_s. \tag{2.7}$$

The boundary on the left edge is the zero Neumann boundary condition

$$\boldsymbol{n}\times(\mu_r^{-1}\nabla\times\boldsymbol{E})=0. \tag{2.8}$$

2.3 Weak formulation of the time-harmonic Maxwell's equation

The weak formulation of Maxwell's equation in Eq. (2.5) is now stated for finite element approximation. Multiplying Eq. (2.5) by a smooth complex vector-valued test function F and integrating over the domain Ω gives

$$\begin{aligned}&\int_\Omega \mu_r^{-1}(\nabla\times\boldsymbol{E})\cdot(\nabla\times\bar{\boldsymbol{F}})dx-\int_\Omega\Big(k^2\varepsilon_r-i\gamma k\sqrt{\frac{\mu_0}{\varepsilon_0}}\Big)\boldsymbol{E}\cdot\bar{\boldsymbol{F}}dx\\&=-i\omega\int_\Gamma \boldsymbol{J}_s\cdot\bar{\boldsymbol{F}}dS\quad\text{for all }\ \boldsymbol{F}\in\boldsymbol{Q},\end{aligned} \tag{2.9}$$

where

$$\boldsymbol{Q}=\{\boldsymbol{E}\in\boldsymbol{H}(\mathrm{curl},\Omega):\boldsymbol{E}\cdot\boldsymbol{t}=0\ \text{ on }\ \partial\Omega\},$$

and $\bar{\boldsymbol{F}}$ is the complex-conjugate to $\boldsymbol{F}$.

3 Automatic hp-adaptivity strategy using Hermes

The major difference between adaptivity in standard low-order FEM (h-FEM) and adaptivity in hp-FEM is the large number of element refinement options in the latter case. In standard h-adaptivity, elements can only be subdivided in space. Automatic hp-adaptivity in hp-FEM is very different from that in h-FEM. In hp-adaptivity, the polynomial degree of elements can be increased without spatial subdivision, or it can be split into four or two sub-elements and distribute the polynomial degree on the sub-elements through many different ways [8, 12, 15].

Hermes is a free and open-source C++ library that implements adaptive hp-FEM and hp-DG solvers for partial differential equations (PDE) and multiphysics PDE systems. Fig. 2 illustrates several possible refinement candidates for a fourth-order element in Hermes.

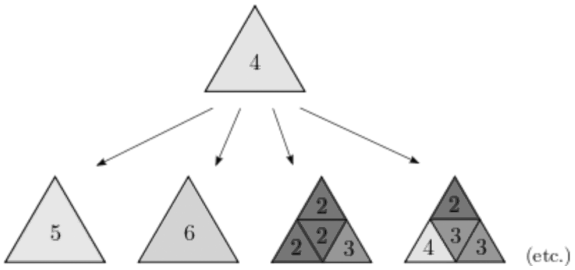

Figure 2: Possible refinement candidates for a fourth-order element in Hermes.

3.1 Adaptivity hp-FEM algorithm in Hermes

With an error estimate of the form

$$\varepsilon_{h,p} \approx E_{ref} - E_{h,p}, \tag{3.1}$$

the outline of our hp-adaptivity algorithm is as follows:

Step 1 To assume an initial coarse mesh $\tau_{h,p}$ consisting of quadratic elements. The maximum allowable range of error in the solution process is $TOL > 0$ for the H(curl) norm of the approximate error function, and the maximum degree of freedoms for hp-adaptivity step is D_{DOF}.

Step 2 To select a coarse mesh as a refinement object and calculate the approximate solution of electric field $E_{h,p} \in Q_{h,p}$ on $\tau_{h,p}$.

Step 3 To calculate the reference solution $E_{ref} \in Q_{ref}$, where Q_{ref} is obtained by dividing all elements and increasing the polynomial degrees by one.

Step 4 To construct the approximate error function, calculate its $\|\cdot\|_A$ norm ERR_i on every element K_i $(i = 1, 2, \cdots, n)$ in the mesh. To calculate the global error,

$$ERR^2 = \sum_{i=1}^{n} (ERR_i)^2.$$

Step 5 If $ERR \leq TOL$, stop computation and proceed to postprocessing. Otherwise, sort all elements into a list of L by the descending order of ERR_i.

Step 6 If the number of degree of freedoms increased at this step is $D \leq D_{DOF}$ (to prevent data overflow for excessive calculation amount), we take the next element K to form the list L, and then perform hp-refinement of K.

Step 7 To adjust polynomial degrees on unconstrained edges using the minimum rule.

Step 8 To continue with Step 2.

Hermes supports eight different modes of automatic adaptivity-P_ISO, P_ANISO, H_ISO, H_ANISO, HP_ISO, HP_ANISO_P, HP_ANISO_H, HP_ANISO. The simplest mode is isotropic refinements h-isotropic (H_ISO) with just one refinement option. The most general mode is hp-anisotropic (HP_ANISO) with around 100 refinement candidates for each element. The selection of the hp-refinement mode is where the user can use his a-priori knowledge of the problem to make the computation faster. Among

all considered refinements of K, the algorithm select the one which yields the smallest projection error.

Note that this approach to automatic adaptivity is PDE-independent and works very well for multiphysics PDE systems [14].

4 Numerical simulation

Based on the weak formulation in Eq. (2.9), the problem is considered with a single material on the formation. The geometry, sources, receivers, and materials used in the present study are illustrated in Fig. 3 through a Cartesian coordinate. A transmitting coil is located at the middle of the formation. When the loaded surface current is not zero, the problem is reduced to an electric field model characterized by an electric field strength E. The solution decays exponentially with the distance from the source [11, 13]. Therefore, the infinite domain can be truncated to the computational rectangular domain shown in Fig. 3; the computational domain of the logging model is set in an 8m $\times$ 6m rectangular domain. In the model, the length of the transmitting coil is 0.1m, the loaded current amplitude of field source is 1.0A, $\varepsilon_r = 10$, $\mu_r = 1$, current transmitter frequency is 100KHz, and electrical conductivity of the formation part is 10S/m.

In Fig. 4, the left and right images are the electric field distribution of the transmitting coil and the final hp mesh, respectively. In the mesh images, the different colors represent the different polynomial degrees of elements.

In Fig. 5, the left image is the real part of the electric field on behalf of the secondary radiation resulting from the reflection from the well, and the right image is the solution

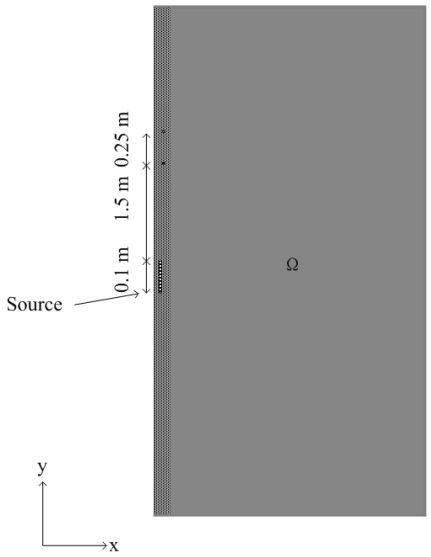

Figure 3: Model consisting of one transmitter, two receiver coils, a conductive borehole, and one layer in the formation material.

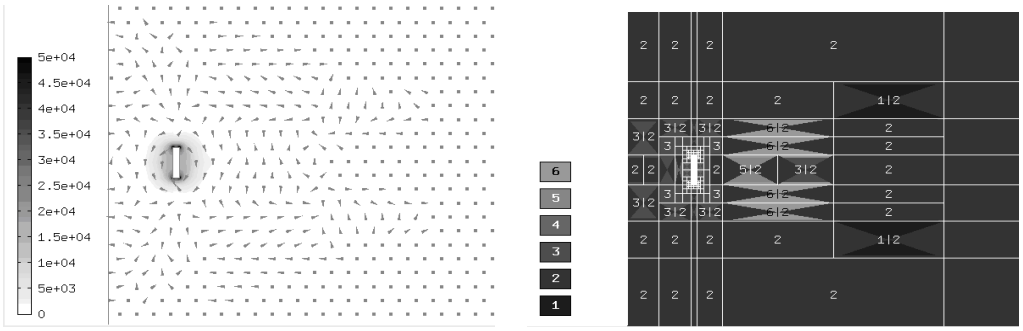

(a) (b)

Figure 4: Electric field distribution (a) and the final hp mesh (b). Zooms on the transmitting coil.

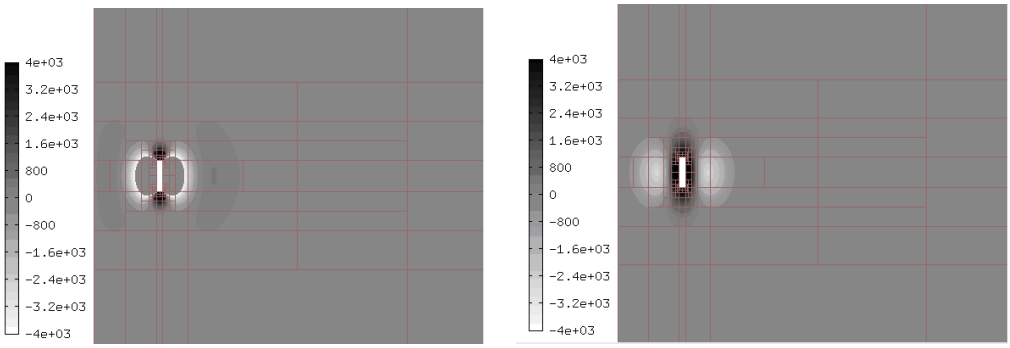

(a) (b)

Figure 5: Radiation from the transmitting coil: zooming on the real (a) and imaginary (b) parts of the solution.

corresponding to the direct radiation from the source.

Fig. 6 shows the relationship between the amplitude of electric field measured in the first receiver coil and its located formation resistivity under different transmission frequencies. Fig. 6 indicates that at the same frequency, the signal strength of the electric field measured in the receiver coil gradually increases with increasing formation resistivity. At the same formation, the signal strength of electric field measured in the receiver coil gradually decreases with increasing emission frequency, which is consistent with the actual condition of instruments.

Fig. 7 shows the convergence curves of the two kinds of self-adaptive algorithm. The current paper uses the two-mesh iteration method to solve problems. The polynomial degree of the initial mesh for hp-FEM is quadratic, whereas that for h-FEM is linear. The error accuracies of the two curves in the degrees of freedom of 300 are both 84.3565%, which indicates that using coarse mesh and mapping mesh will result in a relatively large initial error in error estimate, and then hp curve will reach the specified accuracy in an exponential convergence rate. Based on the features of the self-adaptive algorithm, mesh refinement around the transmitting coil can propagate in all directions. The mesh dramatically increases around the transmitting coil at $< 1.0\%$

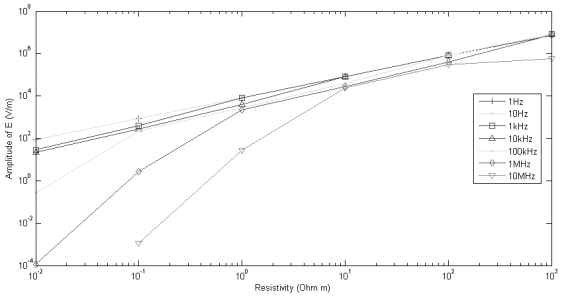

Figure 6: Relationship between formation resistivity and amplitude of the electric field under different transmission frequencies.

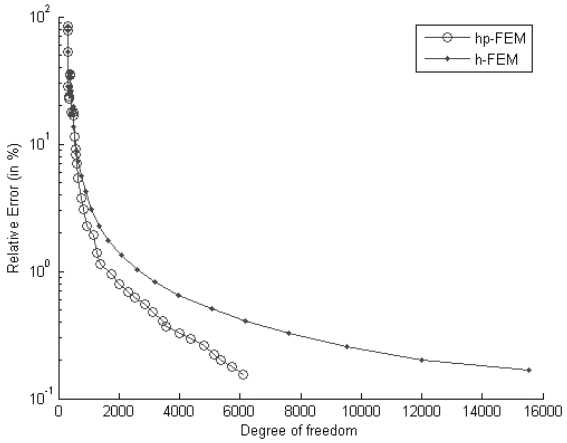

Figure 7: Convergence history.

relative error. Fig. 7 shows that the hp curve can reach 0.1% solution accuracy using only fewer degrees of freedom, which appears as an exponential convergence process. The h curve starts from the same coarse mesh. However, the degrees of freedom's drastic growth is 5% accurate, and the final convergence curve is an algebraic convergence process. The calculation model using the self-adaptive hp algorithm described in Section 3 can result in an exponential convergence rate with a higher accuracy using only relatively few degrees of freedom. Compared with the h algorithm, hp algorithm can significantly decrease the calculated strength and save computing time.

4.1 Multilayered model

The 2D cross-section of the resistivity LWD instrument in a borehole environment is shown in Fig. 1, whose domain, outer boundary conditions, and boundary conditions of transmitting coil are the same as the model of the single-layer formation described in Section 4.1. Multi-frequency LWD tool measurements operating at different frequencies in a borehole environment are simulated for the assessment of rock formation properties. The transmitting coil is located at $(0.05, 10)$ point in the initial state. When the transmitting coil is not fixed, the coil constantly moves along the borehole,

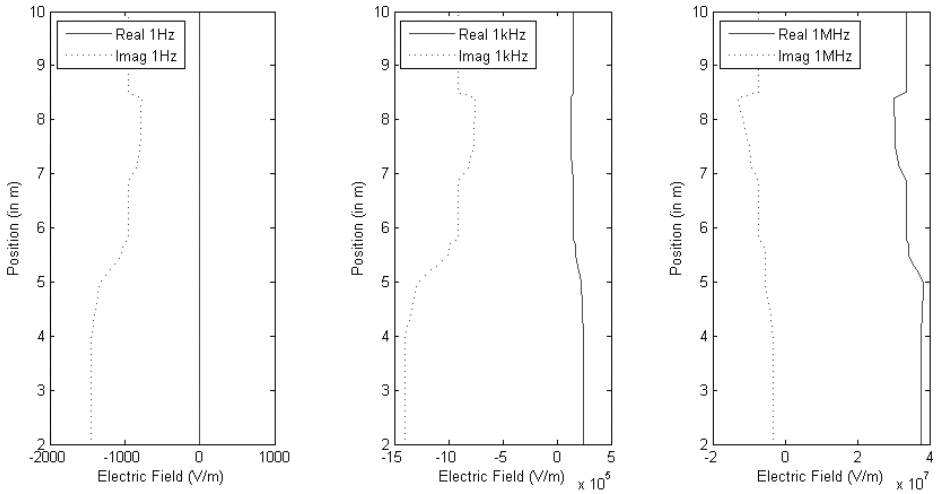

Figure 8: Real part and imaginary part curves of the first receiver coil at 1Hz (a), 1KHz (b), and 1MHz (c) transmitting frequencies.

which is equivalent to the actual process of logging.

Fig. 8 shows the respective electric field curves of the first receiver coil at 1Hz, 1KHz, and 1MHz transmitting frequencies. In the curve with a low frequency of 1Hz, the real part of the electric field is approximately a straight line, and the change in the imaginary part of the electric field reflects changes in formation resistivity. In the curve with 1KHz frequency, the real part of the electric field reflects the formation resistivity changes to some extent. In addition, the imaginary part of the electric field in this curve is similar with that in the curve with 1Hz frequency, wherein the only difference is that its value has an increase of nearly 1,000 times to the right in the direction of the horizontal coordinate. In the curve with a high frequency of 1MHz, the real part of the electric field significantly changes, whereas its imaginary part curve weakens. The changes in the real and imaginary parts of the signals at different frequencies ultimately reflect the amplitude of the electric field signal and change the features of the phase angle.

Fig. 9 shows the signal amplitude curves of the first receiver coil in the formation at different frequencies; the higher the transmitting frequency is, the larger the signal amplitude. However, the changing trend in the curve of receiving signal does not change significantly at different frequencies, implying that the variation rule of signal amplitude has no relationship with frequency.

Fig. 10 shows the signal phase angle curves of the first receiver coil in the formation at different frequencies. The change of phase angle is greatly affected by the real and imaginary parts of the electric field. Therefore, the higher the frequency is, the more apparent the phase angle change will be. This is consistent with the results in Fig. 8.

Comparing the difference value ΔE of the signal amplitudes of the two receiver coils can show the difference value of the signal amplitudes returned by the current

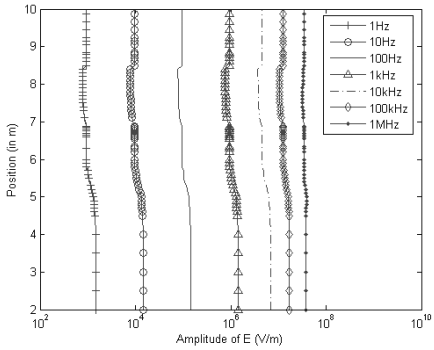

Figure 9: Relationship between amplitude and formation depth.

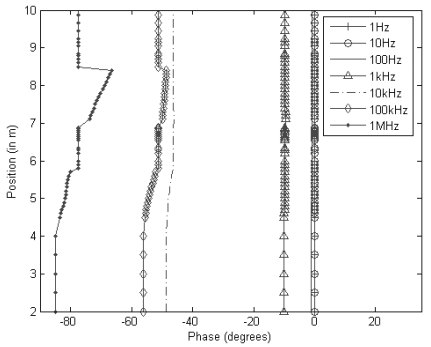

Figure 10: Relationship between phase angle and formation depth.

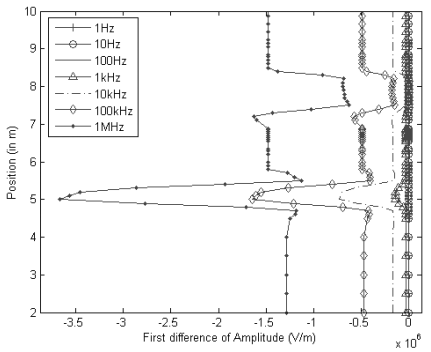

Figure 11: First difference value of amplitude and formation depth curve.

that has entered into formation after passing through the target formation

$$\Delta E = E(y_2) - E(y_1), \tag{4.1}$$

where y_1 and y_2 represent the positions of the two receiver coils, and $E(y_1)$ and $E(y_2)$ represent the signal amplitude of the two receiver coils. Fig. 11 illustrates that a difference value curve of electric field amplitude can clearly distinguish a 0.5m thick thin-layer formation, showing a high-resolution accuracy. In addition, the higher the

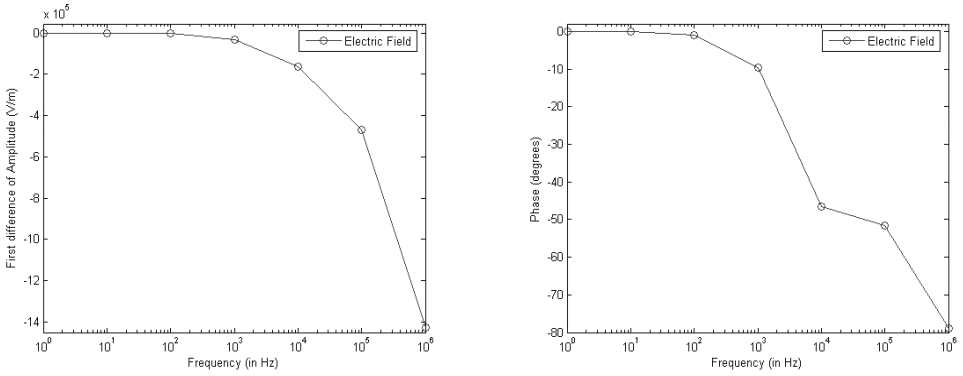

(a) (b)

Figure 12: Effect of frequency on amplitude and phase angle.

frequency is, the larger the signal difference value of the two receiver coils will be. The interface of rock formation is more easily distinguished, and the apparent polarization angle at the interface is observed. Fig. 11 fits well with the actual layering of the model, which proves the accuracy of a self-adaptive *hp*-FEM solution.

Fig. 12 shows the relationship among electric field amplitude, phase angle, and frequency when the first receiver coil is located at a depth of 6m. The electric field amplitude in Fig. 12(a) shows an exponential decay with increasing transmitting frequency, the result of which is consistent with that in Fig. 8. The electric field phase angle in Fig. 12(b) exhibits a rapid decay with increasing transmitting frequency. The decay process of phase angle on the right graph is more apparent than that on the left.

After solving the electric field E, the amplitude ratio and phase difference between the two receiver coils of the instrument can be obtained according to the integral of the electric field E surrounding the receiver coils $V(R_i) = \oint_{R_i} E(l)dl$

$$\begin{cases} S = \dfrac{|V(R_2)|}{|V(R_1)|}, \\ \Delta\varphi = \arg V(R_1) - \arg V(R_2). \end{cases} \tag{4.2}$$

These two sets of data have corresponding relationships with the formation resistivity near the instrument; therefore, it is widely used in resistivity logging. Currently, the formation resistivities detected by most resistivity logging instruments are obtained based on the conversion of amplitude ratio and phase difference of receiver coils. Fig. 13 describes the amplitude ratio curves of the receiver coils obtained using the instrument.

Fig. 14 describes the phase difference curves of the receiver coils obtained using the instrument.

Electromagnetic waves decay when transmitting information. The lower the formation resistivity is, the faster the decay rate will be. Therefore, the amplitude ratio between the two receiver coils in the low-resistivity layer is greater than that in the

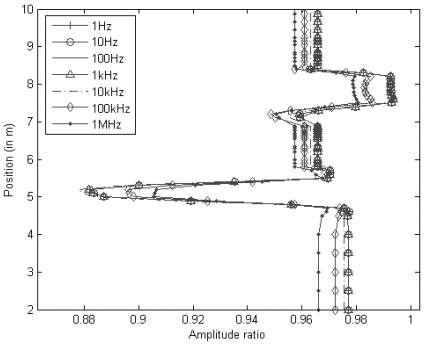

Figure 13: Amplitude ratio.

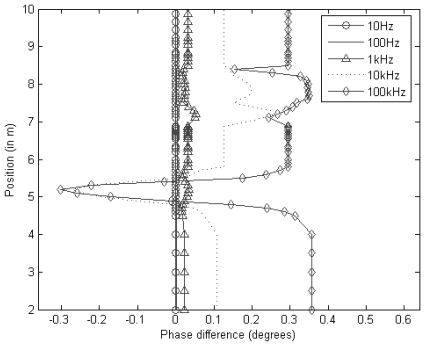

Figure 14: Phase difference.

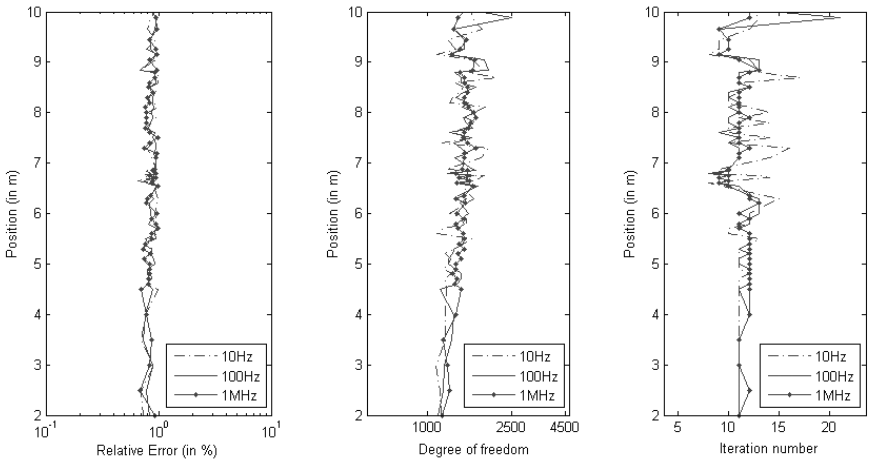

Figure 15: Relative errors, calculated degrees of freedom, and iteration number.

high-resistivity layer. The phase difference value between the two receiver coils is generally inversely proportional to the resistivity of the formation where the instrument is located. That is, the phase difference of the receiver coil at the high resistivity layer is small, whereas that at the low resistivity layer is large.

Fig. 15 shows the relative errors, calculated degrees of freedom, and iteration numbers at three different transmitting frequencies. As the logging instrument move along the borehole, the average error of all the calculated points is less than 0.8%, average degrees of freedom is 2000, and average iteration number is 12. Fig. 7 reveals that the *hp* algorithm used in the present study is highly efficient and accurate, making it more suitable for simulating various types of resistivity logging.

5 Conclusions

The LWD structure and measuring principle of a multi-frequency resistivity logging instrument are presented in the current study. Analysis simulation on resistivity log-

ging models at different frequencies using the novel, highly efficient and accurate self-adaptive *hp*-FEM library Hermes is also reported.

Compared with the commonly used *h* algorithm, the algorithm proposed in the current study can automatically adjust the refinement process according to the actual formation model, which greatly decreases the amount of calculation, obtains accurate approximate solutions of electric field faster, and reduces the requirements on system hardware and memory. The results in Section 4 are highly consistent with those in the actual model, verifying high accuracy and efficiency of the algorithm. The electric field distribution in formation is shown, and the physical meanings of the various logging curves in complex formations are analyzed.

The method proposed in the current paper can be applied to complex calculation models with any thickness formation and can be easily extended to studies on inclined-well models and through-casing resistivity logging models. Electrical logging numerical simulation is the basic tool for electrical logging research, instrument development, and other applications. The existing forward simulation method can improve the accuracy and efficiency of analysis results, which has important practical significance and application values in reducing the cycle of development and application of resistivity LWD instruments.

Acknowledgments

The work for this paper was supported by the National Natural Science Foundation of China under Projects No. 41074099.

References

[1] Z. CHIMEDSURONG AND H. WANG, *Forward modeling of induction well logging tools in dipping boreholes and their response*, Chinese. J. Comput. Phys., 20 (2003), pp. 161–168.
[2] X. CHEN, D. LIU AND Z. MA, *Numerical simulation of electric field in resistivity LWD using High accuracy self-adaptive hp-FEM*, Chinese. J. Comput. Phys., 28 (2011), pp. 50–56.
[3] D. PARDO, *Two-dimensional high accuracy simulation of resistivity logging while drilling (LWD) measurements using a self adaptive goal oriented finite element method*, SIAM. J. Appl. Math., 66 (2006), pp. 2085–2106.
[4] H. O. LEE, Cylindrical FDTD Analysis of LWD Tools Through Anisotropic Dipping Layered Earth Media, M.S. Thesis, The Ohio State University, 2005.
[5] M. TAN, J. GAO, X. WANG AND S. ZHANG, *Numerical simulation of the dual laterolog for carbonate cave reservoirs and response characteristics*, Appl. Geophys., 8 (2011), pp. 79–85.
[6] J. R. LOVELL, Finite Element Methods in Resistivity Logging, Ph.D Thesis, Delft University of Technology, 1993.
[7] Q. CHEN, D. PARDO, H. LI AND F. WANG, *New post-processing method for interpretation of through casing resistivity (TCR) measurements*, J. Appl. Geophys., 74 (2011), pp. 19–25.
[8] L. DUBCOVA, P. SOLIN, J. CERVENY AND P. KUS, *Space and time adaptive two-mesh hp-finite element method for transient microwave heating problems*, Electromagnetics., 30 (2010), pp. 23–40.

[9] T. VEJCHODSKY, P. SOLIN AND M. ZITKA, *Modular hp-FEM system HERMES and its application to the Maxwell's equations*, Math. Comput. Simul., 76 (2007), pp. 223–228.
[10] P. SOLIN, K. SEGETH AND I. DOLEZEL, Higher-Order Finite Element Methods, Chapman & Hall/CRC Press, Philadelphia, 2002.
[11] L. DEMKOWICZ, Computing with *hp*-Adaptive Finite Elements: One and Two Dimensional Elliptic and Maxwell Problems, Chapman & Hall/CRC Press, Boca Raton, 2006.
[12] P. SOLIN, J. CERVENY AND I. DOLEZEL, *Arbitrary-level hanging nodes and automatic adaptively in the hp-FEM*, Math. Comput. Simul., 77 (2008), pp. 117–132.
[13] D. PARDO, L. DEMKOWICZ, C. TORRES-VERDIN AND M. PASZYNSKI, *A self-adaptive goal-oriented hp finite element method with electromagnetic applications, part II: electrodynamics*, Comput. Methods. Appl. Mech. Eng., 196 (2007), pp. 3585–3597.
[14] P. SOLIN, J. CERVENY, L. DUBCOVA AND D. ANDRS, *Monolithic discretization of linear thermoelasticity problems via adaptive multimesh hp-FEM*, J. Comput. Appl. Math., 234 (2010), pp. 2350–2357.
[15] P. SOLIN, L. DUBCOVA, J. CERVENY AND I. DOLEZEL, *Adaptive hp-FEM with arbitrary-level hanging nodes for Maxwell's equations*, Adv. Appl. Math. Mech., 2 (2010), pp. 518–532.